Advanced Materials

ADVANCED MATERIALS
www.advmat.de

RESEARCH ARTICLE

Inhalable Respiratory Driven Penetration of Porous Microsphere-Based Mucosal Vaccine for Long-Term Immune Protection

Zhisheng Xiao[1,2,3] | Zhiqiang Wu[1] | Qiaofeng Li[2] | Jiafei Zhu[2] | Bo Liu[2] | Yu Miao[2] | Yifan Yang[2] | Junjie Zhu[1] | Linfu Chen[2] | Boxiong Bai[2] | Feng Pan[1] | Yang Yang[1,3] | Qian Chen[2]

[1]Department of Thoracic Surgery, Shanghai Pulmonary Hospital, School of Medicine, Tongji University, Shanghai, China | [2]Institute of Functional Nano & Soft Materials (FUNSOM), Jiangsu Key Laboratory for Carbon-Based Functional Materials and Devices, Soochow University, Suzhou, China | [3]Department of Thoracic Surgery, The Fourth Affiliated Hospital of Soochow University, Suzhou, Jiangsu, China

Correspondence: Yang Yang (timyangsh@tongji.edu.cn) | Qian Chen (chenqian@suda.edu.cn)

Received: 2 December 2025 | **Revised:** 11 February 2026 | **Accepted:** 23 February 2026

ABSTRACT

Inhalable mucosal vaccines elicit mucosal immunity non-invasively but are hindered by lung barriers like mucociliary clearance and phagocytosis, which typically necessitate multiple doses. Herein, we developed an innovative inhalable porous microsphere (pMS) vaccine using a single Food and Drug Administration-approved material, featuring a dual-scale design: an aerodynamic diameter of 4.84 μm for optimal deep lung deposition and a geometric size of 14.7 μm to evade phagocytosis for long-term retention. Notably, respiratory motion facilitates the penetration of pMS through the mucus layer into the pulmonary interstitium, where it gradually releases antigens and adjuvants. Remarkably, a single inhalation induced durable immunity, sustaining high levels of IgG and IgA for one year, alongside enhancing tissue-resident memory T cells in the lung and promoting germinal center expansion in the lymph node. This provided long-term protective efficacy, significantly inhibiting lung tumor metastasis even a year after inhalation. Beyond prophylaxis, this vaccine demonstrated remarkable therapeutic efficacy across multiple preclinical models, including the in situ lung tumor model, postoperative recurrence prevention model, and clinically relevant Patient-Derived tumor Xenograft (PDX) model. The dry powder pMS platform is scalable, stable, and clinically translatable, emerging as a versatile therapeutic strategy to adapt to diverse Lung-related diseases.

1 | Introduction

Mucosal vaccines, a category of non-invasive vaccines, offer a painless administration method that reduces healthcare risks and costs, presenting an innovative solution for rapid and scalable immunization during pandemics and outbreaks [1, 2], as they are delivered through mucosal surfaces such as the nose, lung, digestive tract, or reproductive tract [3, 4]. These vaccines can directly elicit a local immune response on the mucosal surface and stimulate the mucosa-associated lymphoid tissue (MALT) [5]. Compared to traditional vaccines, mucosal vaccines have distinct advantages, including the ability to activate effective mucosal immunity in situ and induce systemic immunity. However, challenges remain due to the dense mucus barrier and high concentration of macrophages at mucosal sites [6, 7], which hinder effective antigen delivery and immune activation by standard vaccine formulations.

Current strategies in mucosal vaccine development focus on enhancing mucus penetration [8–13] and incorporating potent adjuvants [14–19] to boost mucosal immune activation. While these methods improve antigen delivery and temporarily enhance immune responses, they fail to fully circumvent the rapid clearance of antigens at mucosal sites, leading to the need for repeated

doses to maintain protective immunity. Additionally, the durability of mucosal immunity remains insufficiently addressed. The complexity of these formulations also poses challenges for large-scale manufacturing, stability, and cost-effectiveness. Therefore, advancing mucosal vaccines that achieve long-lasting immune activation with single-dose administration, while maintaining formulation simplicity, represents a critical priority.

In this work, we developed a breathing-driven, inhalable porous microsphere (pMS) mucosal vaccine using Food and Drug Administration (FDA)-approved poly(lactic-co-glycolic acid) (PLGA) materials, designed for scalability in large-scale manufacturing (Figure 1a). By precisely engineering the geometric and aerodynamic particle sizes, these pMS are capable of deep lung deposition upon inhalation and exhibit prolonged retention in the lower respiratory tract for up to 30 days. Notably, beyond the initial inertial-driven mucus impaction, the pMS leverage respiratory motion to penetrate the mucus layer and translocate into the pulmonary interstitium. This unique delivery mechanism, coupled with the sustained release of antigens and adjuvants, elicits robust and durable mucosal immunity. Remarkably, the pMS vaccine-maintained antigen-specific antibody titers for up to one year and demonstrated protective efficacy in the lung tumor metastasis model even one-year post-inhalation. Furthermore, the vaccine effectively activated immune responses in the lung, increasing tissue-resident memory T cells by 5.4-fold compared to the free group, and promoted germinal center formation in nearby MALT. Through comprehensive preclinical evaluation, the pMS vaccine has demonstrated potent inhibitory effects on both tumorigenesis and progression across multiple tumor models, including orthotopic lung tumor models, post-resection metastasis prevention paradigms, and clinically representative Patient-Derived tumor Xenograft (PDX) models that closely mimic human disease pathophysiology.

2 | Preparation and Characterization of pMS

The porous microspheres (pMS) were prepared by the classic double emulsion method, where pore formation was induced by adding a higher protein concentration to the inner aqueous phase. This increased osmotic pressure allowed liquid ingress during the solvent volatilization process. After solidification, the pMS were lyophilized to ensure stability and suitability for long-term storage (Figure 1b). The emulsion method's precisely controllable scaling capacity facilitates large-scale manufacturing of pMS while maintaining product consistency (Figure 1c). Microscopy images revealed the intricate, opaque internal structure of pMS (Figure 1d), in contrast to the homogeneous interior of non-porous microspheres (Figure S1). Scanning electron microscopy (SEM) further characterized the morphological features of pMS. As shown in Figure 1e, the pMS exhibited a uniform size distribution with visible porous on their surface. Size distribution analysis using a Laser Scattering Particle Size Distribution Analyzer determined the average geometric particle size of the pMS to be approximately 14 μm, which is larger than the phagocytic size limit for macrophage [20–22] (Figure 1f). By measuring the vibrational density of the microspheres as 0.118 g/cm^3, the aerodynamic particle size was calculated to be 4.84 μm. Particles with aerodynamic particle sizes below 5 μm are known to have superior lung deposition efficiency [23, 24]. Additionally, the physical properties of the pMS made them suitable for aerosol formation using a dry powder insufflator, optimizing delivery efficiency in the spray direction (Figure 1g).

We then systematically investigated the biocompatibility of pMS. Initially, various concentrations of pMS were co-cultured with dendritic 2.4 (DC 2.4) cells and murine lung epithelial-12 (MLE 12) cells for 24 h, and the cell viability was evaluated using the standard 3-(4,5-dimethylthiazol-2-yl)-2,5-diphenyl tetrazolium bromide (MTT) assay (Figure S2a,b). The results showed negligible cytotoxicity across both cell lines, even at the highest concentration of 1 mg/mL, indicating excellent in vitro biocompatibility. To further assess biocompatibility in vivo, lung function was evaluated after mice inhaled pMS at the dose of 50 mg/kg. It was found that their respiratory rate and arterial O_2 saturation were nearly identical to those of healthy mice over the course of a month (Figure 1h,i). After 30 days, the mice were sacrificed, and their lungs were subjected to hematoxylin-eosin (H&E) staining. As expected, the inhaled pMS exhibited nearly no detrimental effects on lung physiology over the 30-day period (Figure S3a,b). Collectively, these results confirm the excellent biocompatibility of pMS both in vitro and in vivo, establishing it as a promising and safe candidate for further vaccine development.

Developing long-term extended-release vaccines is a promising strategy to minimize the number of required doses, making it essential to understand in vivo behavior of the carrier. To validate the deep lung deposition of pMS, mice were administrated Cy5.5-labeled nonporous microspheres (nMS) and pMS with identical geometric diameters using a dry powder insufflator. One-hour post-inhalation, the mice were sacrificed, and their lungs were collected for imaging to analyze microsphere distribution. It was found that nMS, due to their larger aerodynamic diameters, showed limited movement by airflow, leading to deposition primarily in the bronchi. In contrast, pMS, with smaller aerodynamic diameters, were dispersed throughout the lungs, demonstrating their ability to reach deeper lung regions under airflow (Figure 2a).

To evaluate the retention ability of pMS, mice were inhaled with Cy5.5-labeled pMS and a nMS with the same aerodynamic diameter. At predetermined intervals post-administration, the mice were sacrificed, and their lungs were collected for imaging to evaluate microsphere retention (Figure 2b–d). On day 7, the pMS group exhibited widespread fluorescence throughout the lung, unlike the limited bronchi-specific fluorescence in the nMS group. The fluorescence images indicated that the radiant efficiency in the pMS group was 6.58 times higher than that in the nMS group. Additionally, quantitative fluorescence analysis of lung lysates demonstrated strikingly enhanced pulmonary retention in pMS-treated groups, with an 8.02-fold greater whole-lung fluorescence intensity (mean percent inhaled dose per gram of tissue (%ID/g)) compared to the nMS group. Notably, on day 21, pMS group maintained sustained pulmonary deposition, retaining 7.62% ID/g (54.24% of the day 7 levels), while the nMS-treated lungs showed no detectable signals. Laser confocal microscopy of lung slices confirmed the extensive distribution of pMS within lung tissue on both days 7 and 21 (Figure S4). To investigate the mechanism underlying the prolonged lung retention of pMS, Cy5.5-labeled nMS and pMS were co-cultured

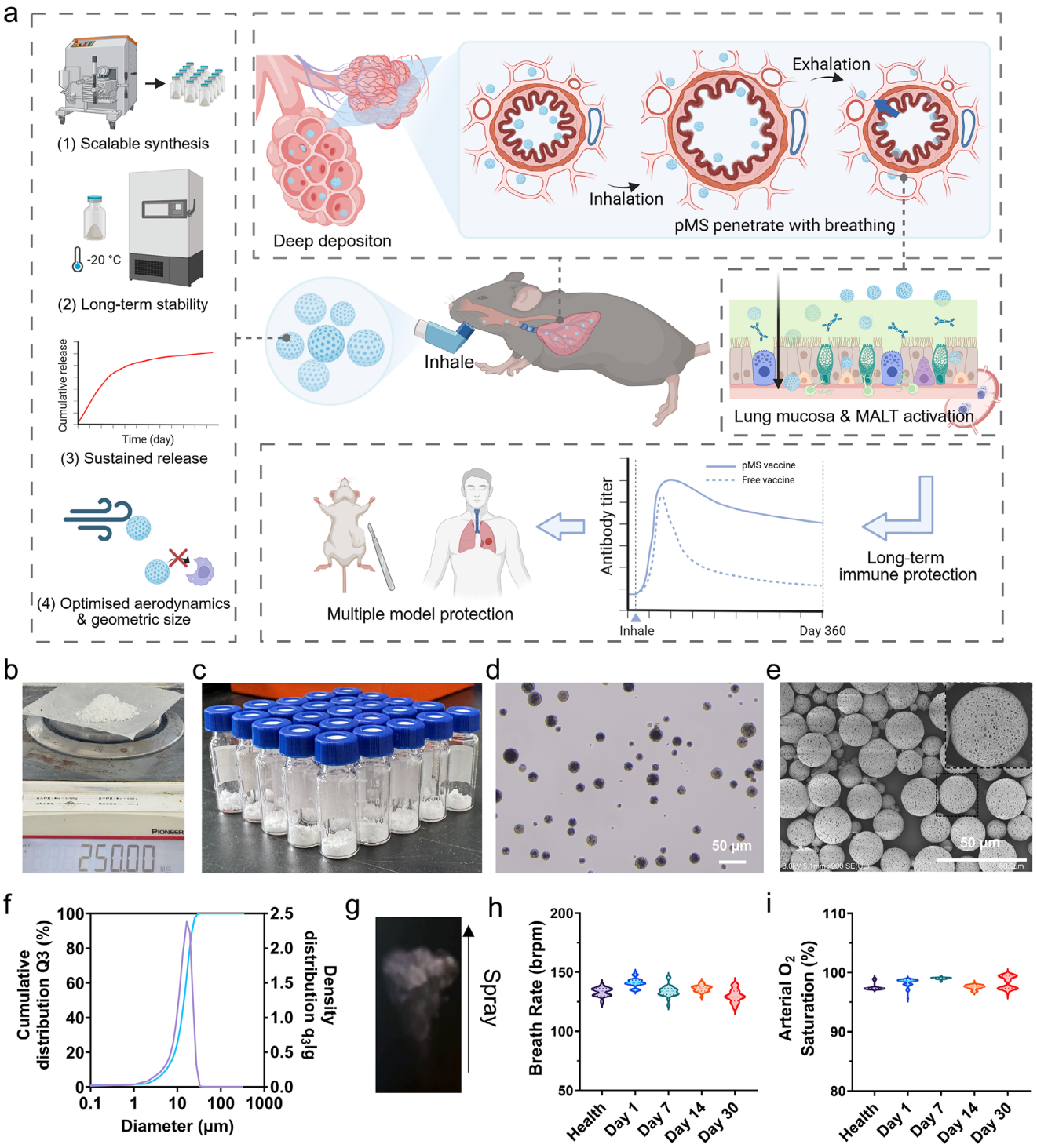

FIGURE 1 | Preparation and characterization of pMS (a) Schematic illustration highlights the advantages of the inhalable, breath driven porous microsphere (pMS). Utilizing natural breathing processes, the pMS effectively penetrates the mucus barrier and integrates into lung tissue, facilitating a pro-longed systemic immune response. (b) Photographs of the lyophilized pMS powders. (c) Images showing the large-scale preparation of pMS. (d and e) Microscopy (d) and SEM (e) images of the pMS. (f) Graph showing the size distribution of pMS. (g) Visual representation of aerosolized pMS produced by dry powder insufflators. (h and i) The breath rate (h) and arterial O_2 saturation levels (i) in mice after inhalation of pMS at different time points.

with the macrophage cell line Raw 264.7, as macrophages are abundant in lung tissue. nMS with smaller geometric diameters were readily endocytosed by Raw cells, whereas pMS with larger geometric diameters were more challenging for the cells to uptake (Figure 2e). Flow cytometry further confirmed this, showing a higher microsphere intensity in Raw cells co-cultured with a nMS, indicating increased uptake (Figure 2f,g). These findings suggest that pMS, with a small aerodynamic diameter and a large geometric diameter, can achieve deep lung deposition and prolonged retention following inhalation.

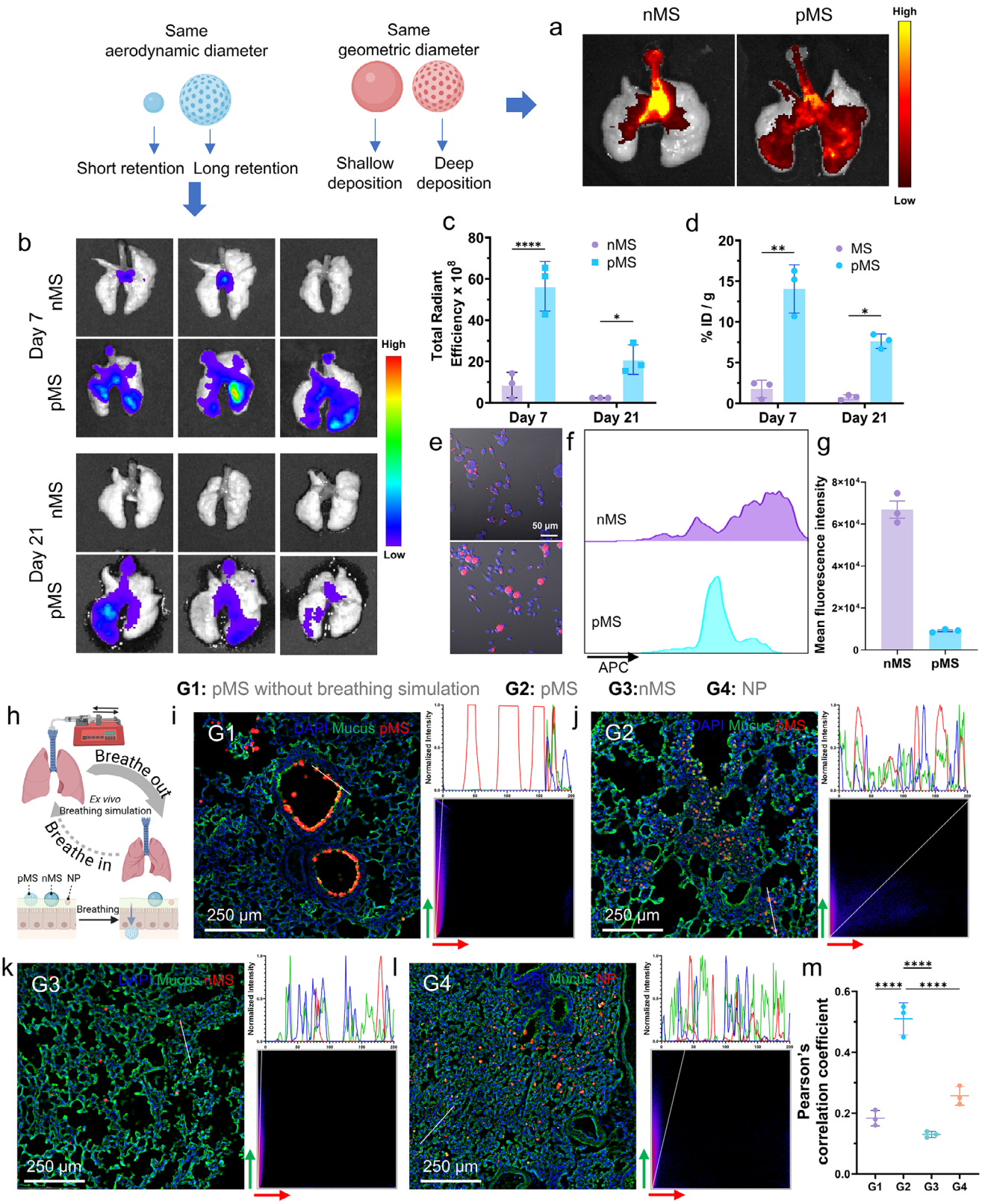

FIGURE 2 | Dynamics of pMS in lung tissue. (a) Ex vivo fluorescence image of the lung one-hour post-administration, comparing nonporous microspheres (nMS) and pMS with identical geometric diameter. (b–d) Ex vivo fluorescence images (b) and semiquantitative analysis (c) of total radiant efficiency, and mean percent inhaled dose per gram of tissue (%ID/g) of lung deposition (d) at 7- and 21-days post-administration for nMS and pMS with equivalent aerodynamic diameters ($n = 3$). (e–g) Confocal fluorescence images (e), flow cytometry plots (f), and statistical analysis (g) of RAW 264.7 cells co-cultured with nMS and pMS with the same aerodynamic diameter ($n = 3$). (h) Schematic illustration of the *ex vivo* breathing simulation process. (i–l) Confocal fluorescence image (left), normalized fluorescence intensity statistics along the white line (top right) and scatterplot of mucus and microsphere or nanoparticle (bottom right) from lung tissue slices under four experimental condition: (i) pMS inhalation without breathing simulation,

In particular, 21 days post-inhalation, lung slides revealed a uniform distribution of pMS throughout the lung tissue, not only within the alveoli but also appearing in the interstitium. This observation piqued our interest, prompting further investigation. The mucosa was stained with wheat germ agglutinin (WGA), proving that the pMS had penetrated the mucosal barrier and entered the interstitial space (Figure S5). Macrophage staining showed no colocalization between macrophages and pMS, demonstrating that macrophage phagocytosis was not responsible for the translocation of pMS to the lung interstitium (Figure S6). Given the unique physical properties of pMS, we hypothesized that respiratory motion might facilitate the translocation of pMS cross the mucus into the lung parenchyma. To test this hypothesis, ex vivo breathing stimulation was performed. Following extraction, the lungs were immediately cannulated via the trachea and connected to a syringe pump. To preserve physiological architecture, the organs underwent cyclic inflation-deflation simulating natural ventilation before processing for precision slicing and subsequent imaging. (Figure 2h; Figure S7). As illustrated in Figure 2i, when mice inhaled pMS and sacrificed within 15 min without breathing stimulation, the pMS were primarily distributed in the airways and alveoli. Fluorescence intensity indicated minimal colocalization with the mucus, probably due to inertial impaction during inhalation causing some pMS to adhere to the mucus. However, following ex vivo breathing stimulation (Figure 2j), pMS penetrated the lung parenchyma, with fluorescence intensity and scatterplots showing significant colocalization of mucus and pMS, indicating that the mechanical forces of breathing facilitate the penetration of pMS through the mucus into the lung parenchyma. In contrast, nMS with the same aerodynamic diameter (4.20 μm) (Figure 2k) and PLGA nanoparticle (NP, 164.2 nm) (Figure 2l) exhibited complete retention within the mucus without detectable penetration, likely due to insufficient inertial momentum for effective mucus transit. The Pearson's correlation coefficient further supported this finding, showing the highest colocalization of mucosa and pMS after breathing stimulation (Figure 2m). These results strongly suggest that, driven by respiratory motion, pMS can effectively penetrate mucus and enter the lung interstitium, making pMS a suitable carrier for inhalable mucosal vaccines.

3 | Construction and Immune Stimulation of pMS Vaccine

To evaluate the potential of pMS as a vaccine carrier, we investigated its antigen-loading capability using ovalbumin (OVA) as a model antigen. During the preparation process, the antigen was successfully encapsulated within the pMS, achieving a loading capacity of 20.3 ± 4.3%. This encapsulation was verified through laser confocal microscopy, which demonstrated the co-localization of Fluorescein 5-isothiocyanateFITC-labeled ovalbumin (FITC-OVA) with Cy5.5-labeled pMS (Figure S8). To further explore the antigen release kinetics, OVA-loaded pMS were immersed in phosphate-buffered saline (PBS) to mimic physiological conditions. The results indicated a gradual degradation of the pMS (Figure S9), with the cumulative release profile showing a sustained release over a period of at least 30 days (Figure S10). For the formulation of a complete vaccine, monophosphoryl lipid A (MPLA), a Toll-like receptor 4 (TLR4) agonist, was incorporated into the pMS system, with a loading capacity of 0.1%, highlighting the potential of pMS as a versatile platform for preparing a vaccine. Moreover, MTT assays demonstrated that even at high concentrations, pMS co-loaded with antigen and adjuvant exhibited negligible cytotoxicity to DC2.4 cells, confirming its excellent biocompatibility (Figure S11).

To investigate the immunostimulatory effects of pMS vaccine, several formulations including pMS encapsulating antigen (pMS(OVA)) (250 μg microspheres, 50 μg OVA), pMS encapsulating adjuvant (pMS(MPLA)) (250 μg microspheres, 0.25 μg MPLA), free antigen and adjuvant (MPLA+OVA) (0.25 μg MPLA and 50 μg OVA), pMS encapsulating both antigen and adjuvant (pMS(MPLA+OVA)) (250 μg microspheres, 0.25 μg MPLA, 50 μg OVA), and the positive control lipopolysaccharide (LPS) (1 μg), were incubated with bone marrow-derived dendritic cells (BMDCs). The maturation markers CD80 and CD86 were evaluated using flow cytometry (Figure S12a,b). The presence of MPLA in pMS(MPLA), MPLA+OVA, and pMS(MPLA+OVA) significantly promotes dendritic cell (DC) maturation by upregulating CD80 and CD86 expression levels. Additionally, increased secretion of pro-inflammatory cytokines interleukin-6 (IL-6), tumor necrosis factor α (TNFα), and interleukin-12p70 (IL-12p70) confirmed DC maturation following exposure to pMS(MPLA), MPLA+OVA, and pMS(MPLA+OVA) (Figure S12c–e). To assess antigen cross-presentation by BMDCs, BMDCs were incubated with the same formulations. Flow cytometry revealed enhanced the highest expression of the SIINFEKL peptide, a specific sequence of OVA, on the surface of BMDCs treated with pMS(MPLA+OVA) (Figure S12f), likely due to enhanced uptake by DCs in the presence of some small microspheres. These results suggest that pMS(MPLA+OVA) effectively promotes DC maturation and triggers subsequent immunological responses, whereas pMS(MPLA) only induced DC maturation without activating the specific immune response due to the absence of antigen. Encouraged by the successful induction of DC maturation and antigen cross-presentation by pMS(MPLA+OVA), we further assessed its ability to induce antigen-specific T-cell responses. Splenocytes from OT-1 mice were extracted, pre-stained with carboxyfluorescein succinimidyl ester (CFSE), and then incubated with BMDCs pre-treated with OVA, pMS(OVA), pMS(MPLA+OVA), and MPLA+OVA to evaluate proliferation. As anticipated, effective proliferation of OT-1 $CD8^+$ T cells was observed in pMS(MPLA+OVA) and MPLA+OVA groups, indicating the successful preparation of the pMS vaccine (Figure S12g,h). For ease of transportation and storage, the pMS vaccine was lyophilized and preserved as a dry powder. After 20 months

(j) pMS inhalation with breathing simulation, (k) inhalation of nMS with same aerodynamic diameter under breathing simulation, and (l) inhalation of PLGA nanoparticle (NP) with breathing simulation. (m) Pearson's correlation coefficient of mucus (green) and microsphere or nanoparticle (red) in different groups ($n = 3$). The data are presented as mean ± SD, and p values were calculated by one-way ANOVA with Tukey's post hoc test, $^*p < 0.05$, $^{**}p < 0.01$, $^{***}p < 0.001$, $^{****}p < 0.0001$.

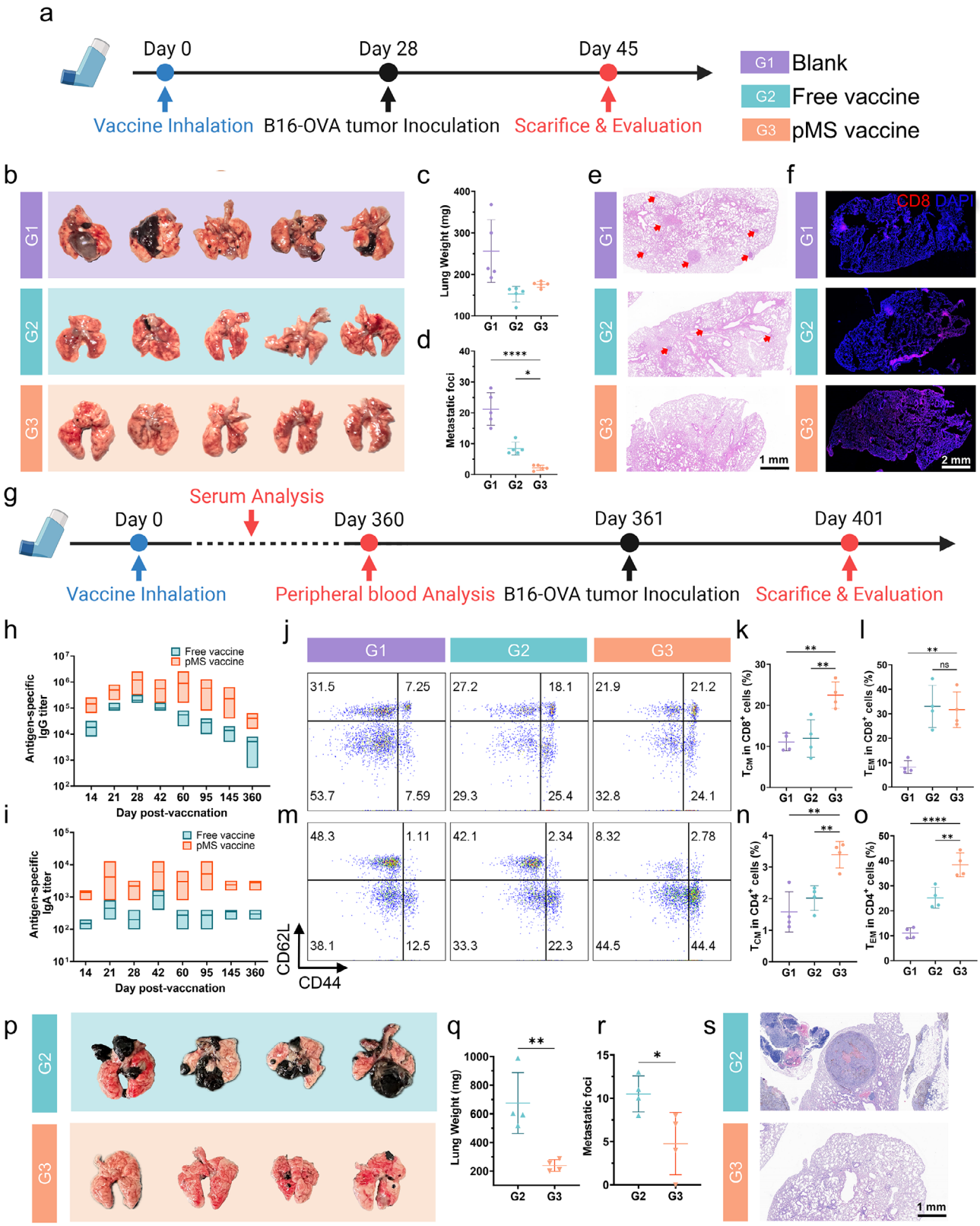

FIGURE 3 | Protective effect of pMS vaccine against lung cancer. (a) Schematic illustration depicting the evaluation of the anti-lung cancer effect of pMS vaccine in C57/BL6 mice. (b–d) The photographs (b), weights (c), and metastatic foci (d) of the lung collected from the different vaccinated mice 17 days post-tumor inoculation ($n = 5$). (e and f) Representative H&E staining (e) and $CD8^+$ immunofluorescence staining (f) of lung slices from mice in different groups. (g) Schematic illustration showing the evaluation of the long-term immune protection effect of pMS vaccine in C57/BL6 mice. (h and i) Antigen-specific IgG (h) and IgA (i) titers in serum at different time points post-vaccination with Free vaccine or pMS vaccine ($n = 4$). (j–l) Representative flow cytometry plots (j) and the relative quantification of center memory T cells ($CD44^+CD62L^+$) and effector memory T cells ($CD44^+CD62L^-$) (l) in $CD8^+$ T cells in peripheral blood ($n = 4$). (m–o) Representative flow cytometry plots (m) and the relative quantification of center memory T cells

of storage at −20°C, the morphology and particle size distribution of the pMS remained nearly unchanged (Figure S13).

To further investigate the in vivo immunostimulatory effects of the pMS vaccine, C57BL/6 mice were inhaled with a combination of free MPLA and OVA solution (Free vaccine) (10 mg/kg antigen and 50 μg/kg MPLA) or pMS encapsulating MPLA and OVA (pMS vaccine) (10 mg/kg antigen and 50 μg/kg MPLA). The mediastinal lymph nodes were collected on day 28 post-immunization for detailed analysis of DC activation. As shown in Figure S14, pMS vaccination elicited significantly increased DC maturation and antigen presentation, indicating that pMS-mediated delivery preferentially activates professional APCs in draining lymph nodes.

To systematically investigate antigen trafficking pathways, we performed dual-modality tracking of fluorescently labeled pMS vaccine components following pulmonary administration. Flow cytometric analysis at day 7 post-inhalation demonstrated efficient antigen uptake by $CD11c^+$ DCs, with ~13% of pulmonary DCs and ~7% of mediastinal lymph node DCs showing antigen-specific fluorescence (Figure S15a–d). Additionally, immunofluorescence microscopy provided spatial confirmation of this process, revealing distinct colocalization of antigen signals with $CD11c^+$ cells in lymph node sections (Figure S15e,f). Further analysis of intact pMS distribution identified a subpopulation of smaller microspheres (~1.5 μm diameter) within lymph nodes, attributing to the size heterogeneity of the microemulsion-fabricated porous microspheres (Figure S16) This observation suggests a dual-phase transport mechanism: the majority of larger pMS (typically >5 μm) remain lung-resident, functioning as sustained-release depots for antigens and adjuvants and a small population of smaller microspheres (~1.5 μm) undergoes DC-mediated transport to the lymph nodes. Moreover, to verify that this formulation did not compromise vaccine efficacy after prolonged storage, both freshly prepared pMS vaccine and pMS vaccine stored at −20°C for six months induced nearly identical immune responses (Figure S17), demonstrating its long-term preservation potential.

4 | Protective Effect Induced by pMS Vaccine Against Lung Cancer Metastasis

Encouraged by the promising advantage of pMS as an inhalable vaccine carrier, we proceeded to explore its potential for preventing lung tumor metastasis. As shown in Figure 3a, C57BL/6 mice were inhaled with the mixture of free MPLA and OVA solution (Free vaccine) (10 mg/kg antigen and 50 μg/kg MPLA) and pMS encapsulating with MPLA and OVA (pMS vaccine) (10 mg/kg antigen and 50 μg/kg MPLA). On day 28, mice received an intravenous injection of 5×10^5 B16-OVA cells, a widely used cancer cell line expressing ovalbumin, to establish the lung metastasis tumor model. To evaluate the vaccine's protective capability against B16-OVA cells, the mice were sacrificed 17 days later, and their lung tumors were collected for different analyses. As exhibited in Figure 3b, significant tumor development was observed in both blank and Free vaccine groups. To quantify the anti-tumor effect, the lungs from different groups were weighed, and the metastatic foci were counted. The pMS vaccine group exhibited a 3.8-fold reduction in metastasis foci compared to the Free vaccine group (Figure 3c,d), indicating the sustained release dosage form provided improved immune protection against cancer cells. H&E staining of retrieved lung tissues further confirmed the anti-tumor effect, revealing nearly no metastasis foci in the pMS vaccine group (Figure 3e). Additionally, immunofluorescence staining was used to assess the distribution of $CD8^+$ T cells in the lung across different groups (Figure 3f). As expected, $CD8^+$ T cells were abundantly distributed throughout the lungs in the pMS vaccine group, whereas other groups exhibited only a sparse presence of $CD8^+$ T cells at the tumor site. Collectively, these results underscore the therapeutic potential of the inhalable pMS vaccine in effectively targeting and mitigating lung cancer. Furthermore, there was no significant change in body weight between the pMS vaccine group and the control group, indicating good biocompatibility of pMS vaccine (Figure S18).

Inspired by the protection effects against lung metastasis and the sustained releasing ability of pMS, we intended to explore the potential for a longer-term immunoprotection effect (Figure 3g). Similarly, the mice were immunized with pMS vaccine and Free vaccine with the same dosage. During one year, blood samples were collected at various intervals and analyzed using the enzyme-linked immunosorbent assay (ELISA) assay to measure serological antigen-antibody titers. It was found that the pMS vaccine group exhibited a more rapid increase in antigen-specific IgG titers, reaching a higher peak and declining more slowly, and maintaining a titer that was 7.8-fold higher on day 360 compared to the Free vaccine group, which may be attributed to the sustained release of immunogenic agents from the microspheres (Figure 3h). Additionally, antigen-specific IgA titers in the pMS vaccine group consistently remained 6.8 to 18.8-fold higher than those in the free antigen and MPLA group (Figure 3i). One year post-vaccination, peripheral blood cells were collected to characterize memory responses. As expected, the percentage of $CD8^+$ and $CD4^+$ central memory T cells ($T_{cm,}$ $CD44^+CD62L^+$) was 1.9-fold ($CD8^+$) and 1.7-fold ($CD4^+$) higher in the pMS vaccine group compared to the Free vaccine group (Figure 3j–o). Inspired by the strong immune memory effect in the pMS vaccine group, we then explored the protective effect against lung metastatic cancer cells. Subsequently, vaccinated mice were intravenously injected with 3×10^5 B16-OVA cells. 40 days later, the mice were sacrificed, and their lungs were collected for further analysis. Compared to the Free vaccine group, the pMS vaccine group demonstrated a significant reduction in metastatic foci, exhibiting 2.2-fold fewer metastatic sites and 2.8-fold lower

($CD44^+CD62L^+$) (n) and effector memory T cells ($CD44^+CD62L^-$) (o) in $CD4^+$ T cells in peripheral blood ($n = 4$). (p–r) The photographs (p), weights (q) and metastatic foci (r) of the lung collected from mice 40 days post-tumor inoculation ($n = 4$). (s) Representative H&E staining slices of lungs collected from the vaccinated mice after tumor inoculation. The data are presented as mean ± SD, and p values were calculated by one-way ANOVA with Tukey's post hoc test, $^*p < 0.05$, $^{**}p < 0.01$, $^{****}p < 0.0001$.

lung weight (Figure 3p–r). The anti-tumor efficiency was further validated by H&E staining of the lung tissues (Figure 3s), which revealed an almost complete absence of metastatic foci in the pMS vaccine group. These results demonstrate that the inhalable pMS vaccine is capable of inducing robust and durable humoral and cellular immune responses lasting up to one year. This promising outcome paves the way for further development of inhalable vaccines that could provide long-lasting immunity against mucosal infections and potentially certain cancers.

5 | Immune Evaluation of pMS Vaccine

The promising effects of pMS vaccine in inhibiting lung cancer progression prompted us to further investigate the underlying mechanism (Figure 4a). C57BL/6 mice were divided into three groups: Blank, Free vaccine, and pMS vaccine (with the equivalent 10 mg/kg OVA, 50 μg/kg MPLA). Given the local T cell activation, we first evaluated the specific immune responses induced by the inhalable pMS vaccine. Splenocytes were isolated 28 days post-vaccination, and effector T cells were analyzed for their secretion of Th1 cytokines, including interleukin-2 (IL-2), and Interferon γ (IFNγ), after antigen stimulation (Figure 4b–e). As anticipated, mice inhaled with the pMS vaccine demonstrated significantly higher levels of IL-2 and IFNγ secreting $CD8^+$ and $CD4^+$ T cells upon antigen stimulation compared to other groups, indicating that the inhaled pMS vaccine induces robust protective cellular immune responses.

This robust activation of splenocytes underscores the potential of pMS vaccine to elicit comprehensive systemic immunity. Beyond systemic effects, delivering the vaccine directly to the lung mucosa—as a mucosal vaccine—holds particular significance by engaging local mucosal immunity, which serves as a critical first line of defense providing rapid and durable protection [3]. To evaluate mucosal immune activation, lung tissues were collected from the vaccinated mice on day 28 post-immunization for in-depth immune cell profiling using flow cytometry. An unsupervised analysis combining uniform manifold approximation and projection (UMAP) for dimensionality reduction with FlowSOM clustering methodology was performed on 11,634 $CD3^+$ T cells. This approach delineated 12 distinct T cell populations based on surface markers (Figure 4f,g). Among these, tissue-resident memory T (T_{rm}) cells—known for their longevity in mucosal tissues and capacity for rapid recall responses upon pathogen re-exposure [25]—were identified as pop11 ($CD8^+CD44^+CD69^+CD103^+$) and pop2 ($CD4^+CD44^+CD69^+$). Notably, only the pMS vaccine group exhibited a clear presence of pop11 in the UMAP visualization alongside a marked elevation in frequency (Figure 4h,i). Similarly, the pMS vaccine group showed a substantial abundance and increased frequency of pop2 cells (Figure 4h,j). Further analysis of CD44 expression— a well-established marker demoting the transition of T cells from a resting to activated states [26]—across total lung T cells corroborated these findings. Specifically, the pMS vaccine group demonstrated a 2.2-fold increase in $CD8^+CD44^+$ T cells and a 3.9fold rise in $CD4^+CD44^+$ T cells compared to the MLPA+OVA group (Figure 4k; Figure S19a,c,d). Moreover, the populations of $CD8^+$ T_{rm} cells and $CD4^+$ T_{rm} cells in this group were elevated by 5.4-fold and 4.9-fold, respectively, relative to the Free vaccine group (Figure 4l; Figure S19b,e,f). These data demonstrate that the sustained release of vaccine components via pMS vaccine not only effectively stimulates activation and proliferation of antigen-specific T cells but also facilitates the establishment and persistence of local T_{rm} populations critical for long-term mucosal immunity. Importantly, measurements of pulmonary IL-6 levels at day 28 post-vaccination revealed no elevation beyond normal physiological concentrations, indicating that our pMS vaccine would not induce chronic inflammation within the lungs (Figure S20).

Inspired by the inhalable pMS vaccine's ability to effectively stimulate and sustain both mucosal and cellular immunity, we sought to evaluate its impact on mucosa-associated lymphoid tissue (MALT). Our focus was particularly on lymph nodes adjacent to mucosal surfaces, where germinal center (GC) reactions occur, playing a crucial role in mediating humoral immunity [27]. On day 28 post-vaccination, we harvested lymph nodes from the mice in different groups, specifically examining the mediastinal lymph nodes adjacent to the lungs. Using laser confocal microscopy, we captured the largest sections of these nodes. As anticipated, the mediastinal lymph nodes in the pMS vaccine group displayed the most pronounced enlargement, characterized by expansive B cell follicles and the largest area of well-organized GC. In contrast, other groups displayed smaller lymph node areas with fewer GC (Figure 4m). To further dissect the immune responses in these lymph nodes, we conducted flow cytometry analysis on cells isolated from the mediastinal lymph nodes. Notably, approximately 4% of $B220^+$ B cells were identified as $CD38^-GL7^+$ GC B cells in the pMS vaccine group, indicating active engagement in the GC stage [28]. This represented a 1.6-fold increase in GC-positive cells compared to Free vaccine groups (Figure 4n,o). Additionally, the proportion of $CD95^+GL7^+$ B cells was also elevated in the pMS vaccine group, further indicating the increasing of GC B cells (Figure S21a). To further characterize GC responses, we analyzed the expression of CD83 (a light zone marker associated with antigen selection and affinity maturation) and CXCR4 (a dark zone marker associated with somatic hypermutation and B cell proliferation) in GC B cells [29]. As shown in Figure 4p, pMS vaccination significantly increased the proportion of $CD83^+$ GC B cells, while CXCR4 expression remained unchanged (Figure S21b), indicating that pMS vaccination preferentially enhances light-zone–associated GC B cell phenotypes, consistent with improved antigen-driven selection and T_{fh} cell interactions. These findings highlight the enhanced humoral immune response facilitated by the pMS vaccine, particularly through robust GC activity and the refinement of antibody quality.

The percentage of follicular helper T cells ($T_{fh,}$ $CXCR5^+CD4^+$ $CD3^+$), which are crucial in regulating humoral immune responses by aiding B cells in producing high-affinity antibodies and maintaining long-term immune memory [30], was 4.6-fold higher in the pMS vaccine group compared to the Free vaccine group (Figure 4q; Figure S21c). Moreover, levels of inducible T-cell co-stimulators (ICOS) (Figure 4r; Figure S21d), which promote B cell activation and maintenance of GC [31], and programmed cell death protein 1 (PD-1) (Figure 4s; Figure S21e), which regulates GC activity to prevent overreaction [32], were

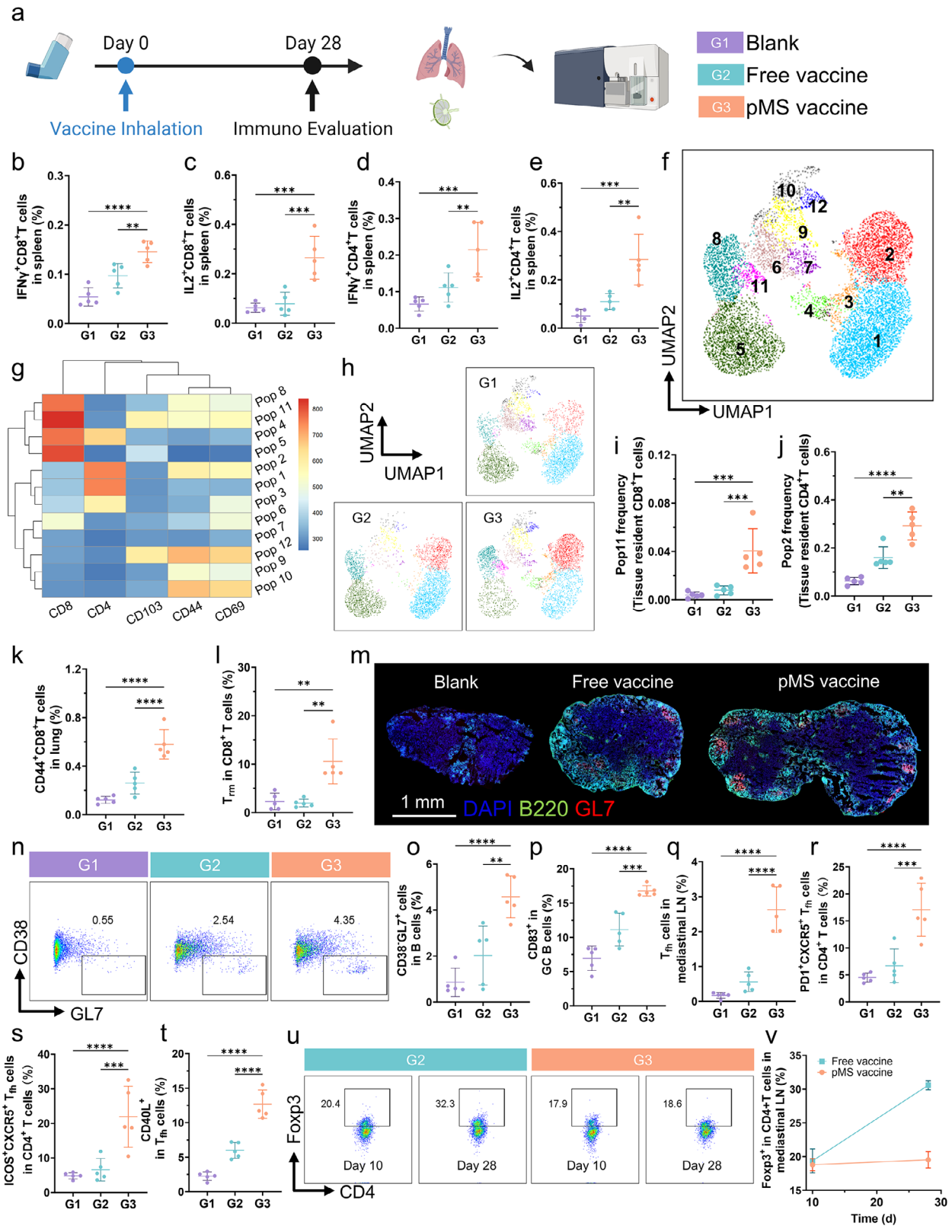

FIGURE 4 | In vivo local immune response stimulated by pMS vaccine. (a) Schematic illustration showing the immune evaluation following a single-dose vaccination in C57/BL6 mice. (b–e) The percentage of IFNγ^+CD8$^+$ T cells (b), IL2$^+$CD8$^+$ T cells (c), IFNγ^+CD4$^+$ T cells (d) and IL2$^+$CD4$^+$ T cells (e) after restimulation of post-immunized splenocytes ($n = 5$). (f) UMAP of 15512 CD3$^+$ cells in the lung tissue across conditions, colored by population membership. (g) Heat map of relative average expression of the marker in each population from Figure 4f. (h) UMAP as in Figure 4f in different groups. (i) Proportion of tissue resident CD8$^+$ T cell (popl1 from Figure 4f) in lung ($n = 5$). (j) Proportion of tissue resident CD4$^+$ T cell (pop2 from Figure 4f) in lung ($n = 5$). (k) Statistical analysis of CD44$^+$CD8$^+$ T cells in lung tissue ($n = 5$). (l) Statistical analysis of tissue-resident memory T cells (CD69$^+$CD103$^+$) in CD8$^+$ T cells in lung tissue ($n = 5$). (m) Representative immunofluorescence staining slices of the mediastinal lymph nodes

significantly increased in the pMS vaccine group. To further characterize T_{fh} cell functionality, we analyzed CD40L expression, a critical co-stimulatory molecule for GC B cell responses [33]. As shown in Figure 4t and Figure S21f, pMS vaccination significantly enhanced CD40L expression on Tfh cells (12.7 ± 2.1%) compared to both the Blank (2.1 ± 0.7%) and Free vaccine (6.1 ± 1.2%) groups. These findings suggest that pMS immunization not only expands T_{fh} cell populations but also functionally augments their capacity to support GC B cell responses through elevated CD40L expression. In the absence of stimulation, $CD4^+$ T cells may differentiate into regulatory T cells (T_r, $FOXP3^+CD4^+CD3^+$), which contribute to GC dissolution [34]. We hypothesized that the robust GC reaction observed in the pMS vaccine group might be attributed to the sustained release of antigen and adjuvant, thereby preventing T_r cell formation. To test this hypothesis, we assessed the kinetics of Foxp3 expression, a marker indicative of T_r cell development, among T cells in both the pMS vaccine and Free vaccine groups at various time points (Figure 4u,v). On day 10, Foxp3 levels were low in both groups were low. However, by day 28, there was a 1.5-fold increase in Foxp3 levels in the Free vaccine group, signifying GC degradation. In contrast, the pMS vaccine group maintained Foxp3 levels consistent with those on day 10, indicating that GC remains active. The decline in GC B cells on day 28 in the Free vaccine group, compared to the stable ratio of GC B cells in the pMS vaccine group, further supports the idea that the sustained release of antigen and adjuvant can prolong the GC reaction (Figure S22a,b).

6 | pMS Vaccine for Treating Multiple Tumor Models

To comprehensively evaluate the broad-spectrum therapeutic potential of the pMS vaccine, we established an in situ lung tumor model by intravenously injecting of luciferase-expressing LLC cells (LLC-Luc) into C57BL/6 mice 5 days post-vaccination. The pMS vaccine was fabricated using cancer cell membrane-derived tumor antigens with pMS serving as the antigen delivery platform. For comparative analysis, we prepared a conventional liposome vaccine encapsulating tumor antigens and adjuvant (Figure 5a). Four treatment groups were evaluated: (1) inhalation of free MPLA and OVA solution (Free vaccine), (2) liposome vaccine administered via conventional intradermal injection (Liposome vaccine (i.d.)), (3) inhalation of liposome vaccine (Liposome vaccine (i.d.)), (4) inhalation of pMS vaccine (pMS vaccine) with an equivalent dose of antigen at 10 mg/kg and MPLA at 50 μg/kg). Tumor progression was monitored through in vivo bioluminescence imaging every 5 days beginning on day 7 (Figure 5b). By day 22, the pMS vaccine group exhibited markedly reduced luminescent signals compared to the Free vaccine and inhaled liposome groups, which exhibited aggressive pulmonary tumor growth. Notably, intradermal administration of the liposome vaccine showed comparable luminescent signals to the blank group, underscoring the limited capacity of the conventional delivery route to induce distal mucosal immunity (Figure 5c). Terminal analysis on day 23 revealed that pMS-vaccinated mice exhibited significantly fewer tumor nodules with a 2.7-fold reduction in tumor mass relative to the liposome vaccine group (Figure 5d,e). Flow cytometry analysis of mediastinal lymph node demonstrated a substantial increase in mature dendritic cell populations in the pMS group (Figure 5f). Tumor-infiltrating lymphocyte profiling showed that the pMS vaccine generated a 1.58-fold greater $CD8^+$ T cell infiltration compared to the liposome vaccine group (Figure 5g; Figure S23a). Furthermore, these tumor-specific $CD8^+$ T cells exhibited functional activation, with $TNF\alpha^+$ and $IFN\gamma^+$ subsets being 1.85-fold and 1.54-fold more abundant, respectively, than those in the liposome vaccine group (Figure 5h,i; Figure S23b,c). These findings collectively demonstrate that while both free vaccine components and conventional liposomal formulations show some antitumor activity, the pMS vaccine platform achieves superior tumor suppression.

Tumor vaccines hold significant promise for preventing postoperative recurrence, a major clinical challenge in cancer therapy. To evaluate this potential, we then established a clinically relevant orthotopic breast tumor model by inoculating luciferase-expressing 4T1 cells (4T1-Luc) into the breast pad of each Balb/c mouse. 9 days post-inoculation, tumors were surgically resected and processed to generate tumor lysates as the source of antigen. We then prepared two vaccine types: the pMS vaccine and a conventional liposomal vaccine. One day post-operation, mice were divided into three groups: inhalation of either liposome vaccine or pMS vaccine (10 mg/kg antigen and 50 μg/kg MPLA), or no treatment (Blank) (Figure 5j,k). Bioluminescence imaging revealed striking differences in metastatic progression: mice in the blank group developed widespread systemic metastasis (with two mice dead by day 21), while liposome-vaccinated mice showed either extrapulmonary metastases (n = 3) or strong pulmonary signals (n = 2). In dramatic contrast, pMS-vaccinated mice exhibited minimal bioluminescence signals, with only one of minor metastasis and two remaining completely tumor-free (Figure 5l). Terminal analysis on day 22 confirmed these findings, with photographs (Figure 5m) and lung weight measurements (Figure 5n) demonstrating near-complete tumor-free in the pMS vaccine group compared to extensive metastasis in both the blank and liposome vaccine groups. Mechanistic studies demonstrated the pMS vaccine's superior immunogenicity, inducing enhanced DC maturation in mediastinal lymph nodes (Figure 5o), increased tumor-infiltrating T cell proportions (Figure 5p; Figure S24a) and profoundly elevated T cell functionality with $TNF\alpha^+$ (Figure 5q; Figure S24b) and $IFN\gamma^+$ (Figure 5r; Figure S24c) cell frequencies 4.58-fold and 2.17-fold higher than liposome vaccine group, respectively. Collectively, these results validated that pMS

in different groups 28 days post-vaccination. (n and o) Representative flow cytometry plots (n) and statistical quantification (o) of $CD38^-GL7^+$ B cells ($n = 5$). (p–t) Percentages of $CD83^+$ GC B cells (Light zone) (p), follicular helper T cells (T_{fh}, $CXCR5^+CD4^+$) (q) $ICOS^+CXCR5^+CD4^+$ T_{fh} cells (r) and $PD1^+CXCR5^+CD4^+$ T_{fh} cells (s) and $CD40L^+CXCR5^+CD4^+$ T_{fh} cells (t) in the mediastinal lymph nodes ($n = 5$). (u and v) Representative flow cytometry plots (u) and statistical analysis (v) of $Foxp3^+CD4^+$ T cells at 10- and 28-days post-vaccination in the mediastinal lymph node ($n = 3$). The data are presented as mean ± SD, and p values were calculated by one-way ANOVA with Tukey's post hoc test, $^*p < 0.05$, $^{**}p < 0.01$, $^{***}p < 0.001$, $^{****}p < 0.0001$.

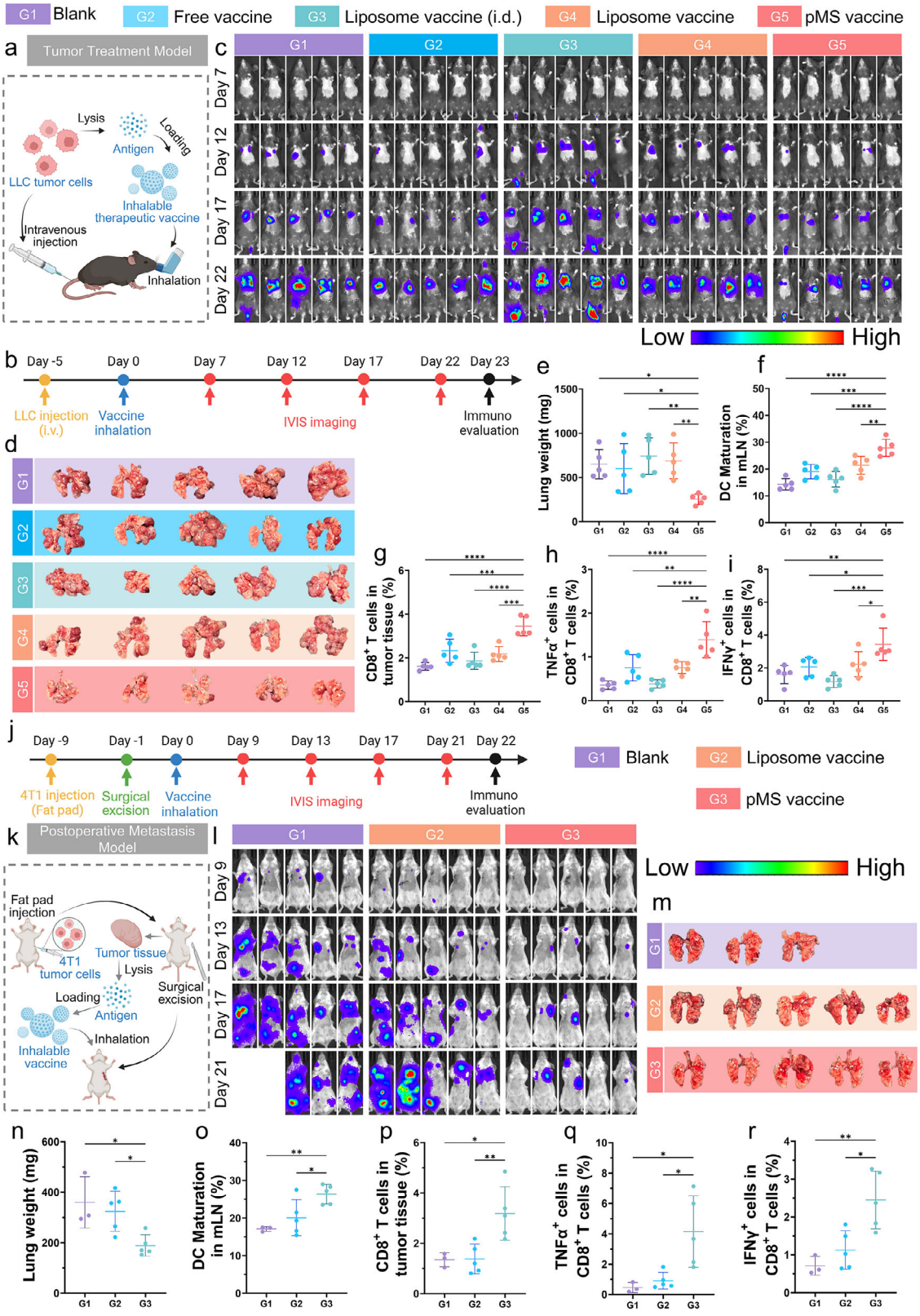

FIGURE 5 | In vivo therapeutic ability of pMS vaccine in different models. (a) The schematic illustration showing the establishment of the LLC local tumor model and the pMS vaccination strategy. (b) The schematic illustration of the experimental schedule of the LLC treatment model. (c) Bioluminescence images of LCC tumor-bearing C57/BL6 mice with different vaccinations. (d and e) The photographs (d) and weights (e) of the lung collected from the different vaccinated mice 23 days post-vaccination ($n = 5$). (f) Statistical analysis of DC maturation 23 days post-vaccination in the mediastinal lymph node ($n = 5$). (g) The statistical analysis shows the percentage of $CD8^+$ T cells in tumor tissue. (g and i) Percentages of $TNF\alpha^+$ (h) and $IFN\gamma^+$ (i) cells in $CD8^+$ T cells in tumor tissue ($n = 5$). (j) The schematic illustration of the experimental schedule of the postoperative metastasis model. (k) The schematic illustration of the establishment of the 4T1 postoperative metastasis model and the pMS vaccination strategy. (l) Bioluminescence

vaccines can potently activate postoperative antitumor immunity and effectively prevent metastatic recurrence.

7 | Therapeutic Efficacy of pMS Vaccine in Humanized PDX Mouse Model

To further assess the clinical translational potential of the pMS vaccine, we investigated its antitumor efficacy using a humanized PDX mouse model. First, we established the humanized immune system in NOD-Prkdc^{scid} Il2rg^{tml}/Cavens mice by intravenous injection of human peripheral blood mononuclear cells (hPBMC) (Figure 6a). Two weeks post-injection, we implanted freshly resected tumor tissues from clinical patients into the axillary region of these mice to generate a humanized PDX model. Simultaneously, the non-transplanted tumor tissue was processed into lysates to serve as the antigen source for vaccine formulation. We compared pMS-based and conventional liposome vaccines administrated via inhalation one day post-tumor transplantation (Figure 6a). Weekly monitoring revealed distinct therapeutic outcomes: while the liposome vaccine showed only transient early-stage tumor suppression, the pMS vaccine demonstrated sustained efficacy, achieving complete tumor eradiation in one case (Figure 6b; Figure S25). Notably, the liposome vaccine group experienced two early deaths (weeks 3–4), potentially due to dose-related toxicity, whereas two late deaths occurred in the untreated group (weeks 8–9) from tumor progression. Terminal analysis at week 11 revealed striking differences: the pMS group exhibited dramatically reduced tumor volumes, with one tumor eliminated and another nearly eradicated (Figure 6c). Quantitative assessment revealed pMS's superior control of tumor growth, showing tenfold versus untreated (127.89 mg) and liposome (71.82 mg) groups (Figure 6d). Flow cytometry analysis of tumor-infiltrating immune cells (n = 3 per group, excluding one nearly cured pMS tumor) demonstrated significantly enhanced CD45$^+$ cell infiltration in pMS-treated mice (Figure 6e,f). This contrasted sharply with the minimal infiltration observed in other groups, suggesting progressive immune exhaustion. Importantly, pMS vaccination specifically boosted CD8$^+$ T cell recruitment, providing mechanistic insight into its sustained efficacy (Figure 6g,h). These results collectively demonstrate the pMS vaccine's exceptional capacity to control patient-derived tumor growth through enhanced immune infiltration, strongly supporting its clinical development potential.

8 | Discussion

The development of inhalable mucosal vaccines represents a promising frontier for non-invasive immunization, yet their efficacy has been consistently hampered by the lung's sophisticated clearance mechanisms—including mucociliary escalation and pervasive macrophage phagocytosis—which collectively limit antigen retention and necessitate repeated administrations [35–37]. While recent advances in nanocarrier design have sought to enhance mucus penetration or incorporate potent adjuvants, such strategies often fall short of enabling durable immune activation from a single dose [38–40]. In this study, we introduce a uniquely engineered porous microsphere (pMS) vaccine that overcomes these limitations through a respiration-enhanced delivery mechanism, enabling sustained antigen presentation and long-term immune protection following a single inhalation.

The pMS vaccine's innovative design centers on its dual-scale architecture: with an aerodynamic diameter of 4.84 μm ensuring optimal deep deposition and a geometric size of 14.7 μm effectively evading phagocytic clearance. Crucially, we discovered that respiratory movements actively drive pMS penetration through the mucus layer into the pulmonary interstitium—a dynamic process unattainable by conventional nanoparticles or non-porous microspheres of comparable aerodynamic size. Once situated in the interstitium, pMS functions as a localized antigen reservoir, enabling sustained release of both antigen and adjuvant for at least 30 days. This prolonged immunostimulation elicited robust systemic immunity, evidenced by persistently high IgG and IgA titers lasting up to one year, alongside potent local mucosal responses, including a 5.4-fold increase in T_{rm} cells and vigorous GC activity in lung-draining lymph nodes. Notably, the pMS vaccine uniquely sustained GC reactions in mediastinal lymph nodes, where extended antigen exposure effectively suppressed Foxp3 upregulation in CD4$^+$ T cells—a mechanism that likely prevents premature GC dissolution and supports prolonged antibody affinity maturation. This persistent GC activity, coupled with elevated T_{fh} cell frequencies, underscores the platform's capacity to elicit not only potent but also qualitatively superior humoral immunity.

Across diverse preclinical models—including lung metastasis, orthotopic lung cancer, postoperative recurrence, and humanized PDX—the pMS vaccine consistently demonstrated superior prophylactic and therapeutic efficacy compared to both free vaccine formulations and conventional liposome-based vaccines. Although conventional liposome-based vaccines showed marginally enhanced efficacy compared to the free vaccine group with improved antigen delivery efficiency, they remained constrained by poor pulmonary retention and typically necessitated repeated administrations. In contrast, the pMS vaccine demonstrated superior immunization efficacy, achieving potent protective immunity with significantly enhanced lung retention and single-dose administration. A single-dose regimen conferred complete protection against tumor metastasis even one-year post-inhalation, highlighting exceptionally durable immunologic memory. Moreover, the vaccine's dry powder formulation, composed entirely of FDA-approved PLGA, ensures excellent storage stability and facilitates clinical translation. The platform's adaptable antigen-loading capacity further enables broad

images of Balb/c mice after surgical resection of tumor tissue and inhalation of different vaccinations. (m and n) The photographs (m) and weights (n) of the lungs collected from the different vaccinated mice 22 days post-vaccination ($n = 5$). (o) Statistical analysis of DC maturation 22 days post-vaccination in the mediastinal lymph node ($n = 5$). (p) The statistical quantification of CD8$^+$ T cells in tumor tissue ($n = 5$). (q and r) Percentages of TNFα^+ (q) and IFNγ^+ (r) cells in CD8$^+$ T cells in tumor tissues ($n = 5$). The data are presented as mean ± SD, and p values were calculated by one-way ANOVA with Tukey's post hoc test, *$p < 0.05$, **$p < 0.01$, ***$p < 0.001$, ****$p < 0.0001$.

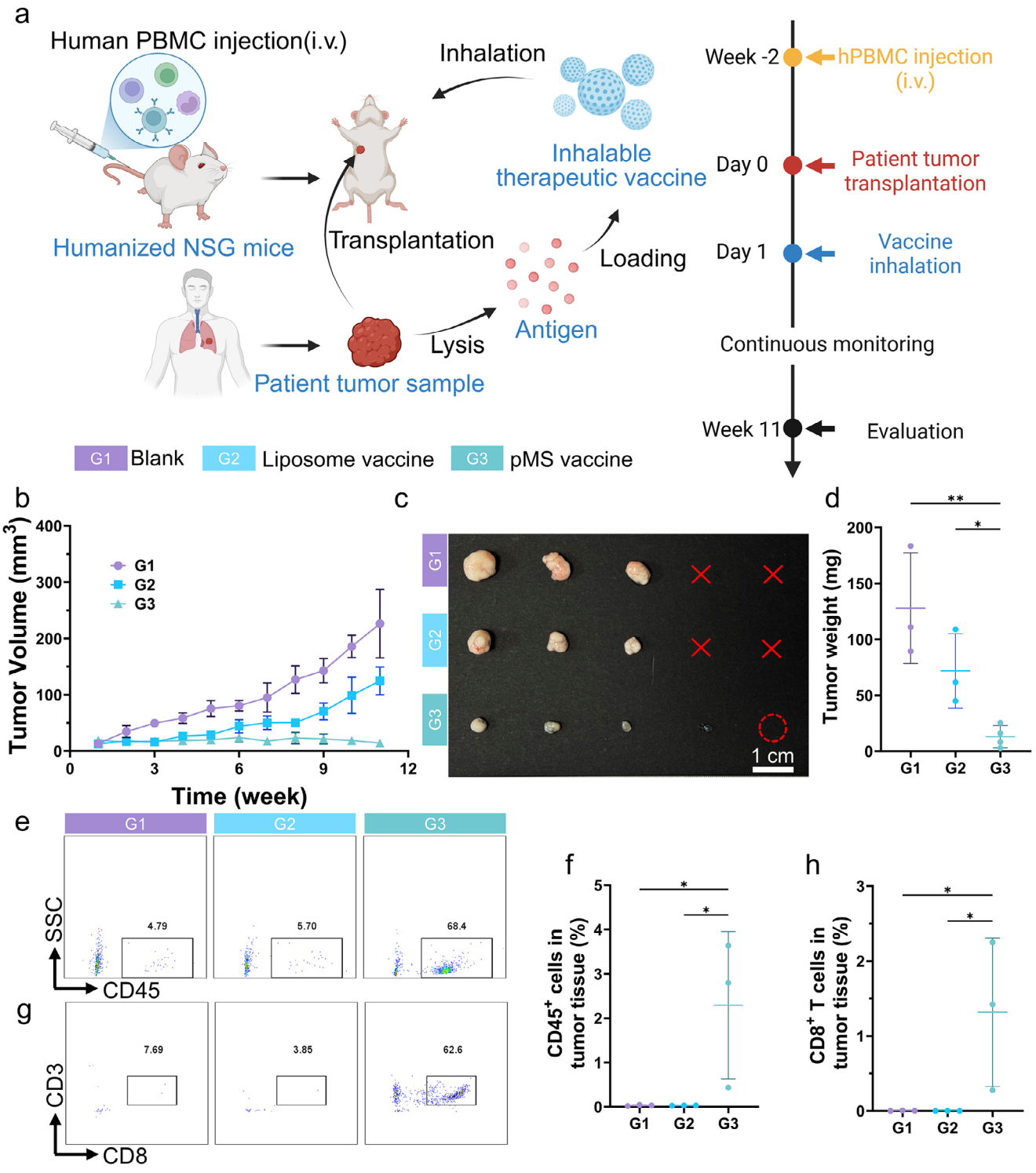

FIGURE 6 | Therapeutic evaluation of pMS vaccine in humanized PDX-bearing mouse model. (a) Schematic illustration and experimental schedule of the establishment of the PDX model on humanized mice and the personalized vaccination strategy. (b) Tumor growth curve of mice after inhalation with different vaccines ($n = 3$ in G1 and G2, $n = 5$ in G3). (c and d) The photograph (c) and weights (d) of the collected tumor tissues after different vaccinations. Scale bar, 1 cm. (e and f) Representative flow cytometry plots (e) and statistical quantification (f) of $CD45^+$ cells in tumor tissues ($n = 3$). (g and h) Representative flow cytometry plots (g) and statistical quantification (h) of $CD8^+$ T cells in tumor tissues ($n = 3$). The data are presented as mean ± SD, and p values were calculated by one-way ANOVA with Tukey's post hoc test, $^*p < 0.05$, $^{**}p < 0.01$.

applicability against various mucosal pathogens or tumor antigens. In summary, this work presents a respiration-driven microsphere platform that integrates deep lung deposition, mucus-penetrating mobility, and sustained immunostimulation to achieve long-lasting mucosal and systemic immunity. By addressing key physiological and immunological barriers in the lung, the pMS vaccine establishes a versatile and clinically translatable strategy for single-dose vaccination against pulmonary infections and malignancies.

9 | Materials and Methods

9.1 | Materials

Poly(lactic-co-glycolic acid) (PLGA, Mw14 kDa) was purchased from Jinan Daigang Biomaterial Co., Ltd. Monophosphoryl lipid A (MPLA) was obtained from Invitrogen (tlrl-mpla). Poly (vinyl alcohol) (PVA-205) and Urea (U755712-500g) were acquired from Aladdin, while ovalbumin (OVA) (A5503-1G) and all other reagents not specified in the experimental section were purchased from Sigma–Aldrich.

9.2 | Cell Lines and Animals

The cell lines MLE12, DC2.4, RAW 264.7, B16-OVA cells, LLC-Luc cells, and 4T1-Luc cellswere obtained from American Type Culture Collection (ATCC), and cultured in DMEM/High glucose (Sperikon Life Science &Biotechnology co., ltd, SP032010500) containing 10% fetal bovine serum (Jin Yuan Kang Biotechnology, JYK-FBS-301), 100 U/mL penicillin, and streptomycin (Procell, PB180120) at 37°C in 5% CO_2 Bone marrow-derived cells (BMDCs) were isolated from C57BL/6 mice and cultured using the standard protocol. Human peripheral blood mononuclear cells (hPBMC) were obtained from Milecell Biotechnology Inc.

Female C57BL/6 mice (6–8 weeks), female Balb/c mice (6–8 weeks), and female NOD-Prkdc^{scid} Il2rg^{tml}/Cavens mice were obtained from Changzhou Cavens Experimental Animal Co. Ltd. OT-1 mice were generously provided by Prof. Z. Liu at Soochow University. All animal experiments were reviewed and approved by the Animals Care and Use Committee of Soochow University (approval ID: SUDA20240724A01). No clinical trial registration number applies to this study, as it is a preclinical investigation using patient-derived xenograft (PDX) models in mice.

9.3 | Fabrication and Characterization of pMS

Porous microspheres (pMS) were prepared by a modified water-in-oil-in-water (w/o/w) double emulsion method, with the inner water phase replaced by a high osmotic solution. Briefly, PLGA (50 mg) was dissolved in methylene chloride (1 mL) and mixed with 0.2 mL deionized water containing 30 mg OVA. The mixed solution was emulsified by a Selecta Sonopuls for 10 s in an ice bath. Then, a 4% PVA solution (7 mL) was added into the emulsion and emulsified using a homogenizer (HR-500DG, Huxi) for 3 min (3000 rpm) at room temperature. The obtained emulsion was poured into 0.4% PVA solution (150 mL) and stirred magnetically for 4 h at 500 rpm at room temperature to evaporate the organic solvent. The solidified pMS were washed three times with deionized water and lyophilized for further use. To prepare MPLA-loaded pMS, 50 μg of MPLA was added to the oil phase before emulsion. Bacterial lysate-loaded pMS and blank pMS were prepared by replacing the inner water phase with bacterial lysate (3.2 mg) and urea (8 M) before emulsion, respectively. Solid microspheres were prepared using the oil-in-water (o/w) emulsion method by directly adding the PLGA-contained oil into PVA solution.

The pMS containing OVA-Cy5.5 in the inner phase and Nile red in the oil phase were characterized using the laser confocal microscope (LSM 800, Zeiss) to confirm the antigen loading. The loading capacity, the pMS was measured by dissolving pMS with NaOH (1 M) and neutralizing with HCl (1 M), following by protein concentration measurement using a BCA protein assay kit (Beijing Boxbio Science & Technology Co., Ltd., AKPR017).

The morphology of pMS was characterized using an inverted research microscope (Ts2R, Nikon) and a field emission Scanning Electron Microscope (SU8230, Hitachi). The size distribution was measured using the Laser Scattering Particle Size Distribution Analyzer (LA-95052, Horiba).

9.4 | Pulmonary Inhalation and Lung Deposition of pMS

Female C57BL/6 mice were anesthetized with isoflurane and fixed with the Mouse Intubation Platform MIP (BJ-P-M, Biojane), and the tracheal openings were visualized using a small-animal laryngoscope (BJ-L, Biojane). Then, lyophilized microspheres (1 mg) were inhaled directly into the lung using a dry powder insufflator (BJ-PW-FM-M, Biojane).

To evaluate lung deposition, mice that inhaled with Cy5.5-labeled microspheres were sacrificed at 1 h, 7 days, and 21 days post-inhalation. The lungs were collected, and the distribution and intensity of microsphere were determined using the in vivo animal imaging system (IVIS Lumina III, Perkin-Elmer). Then, the lungs were divided into two parts. One part was embedded in the optimal cutting temperature (OCT) compound, sectioned using the freezing microtome (CM1860, Leica), and stained with DAPI for confocal imaging. The other part was weighted, lysed using a bead beating grinder and lysis system (FASTPREP-24, Mpbio), and the fluorescence intensity was quantified using the multimode microplate reader (Synergy H1, Bio Tek) to calculate the mean percent inhaled dose per gram (% ID/g).

9.5 | Cellular Uptake of Microspheres

To determine the cellular uptake of pMS, Raw 264.7 cells were seeded in 35 mm confocal dishes (BeyoGold) and 6-well plates at a density of 10^5 cells per well. 12 h later, different Cy5.5 labeled microspheres were added to the dishes or plates and cultured for another 24 h. The uptake microspheres were then characterized with a laser confocal microscope (LSM 800, Zeiss) and flow cytometry (Fongcytes, Challenbio).

9.6 | Ex Vivo Breathing Stimulation

By sacrificing mice inhaling different materials and removing the intact lungs, the main trachea was connected to a syringe on a syringe pump via an indwelling needle and the syringe pump was programmed (500 pushes and pulls back and forth in a 0.5 mL volume) to mimic the respiratory process. The lungs were then sectioned and stained for nuclei and mucus using DAPI and wheat germ agglutinin (WGA). Material and mucus were analysed for colocalization using ImageJ 1.54p and the plugin Colocalization Finder.

9.7 | Antigen Release and pMS Degradation

To evaluate the sustained release of antigen, pMS (2 mg) were suspended in 0.5 mL 1 × PBS containing 0.01% Tween 20, and gently shaken under 37°C. At predetermined time points, the pMS were centrifugated and the antigen content in the supernatant was determined by BCA protein assay kit. To examine the degradation behavior of pMS, Nile red labeled pMS (2 mg) were suspended in 1 mL 1 × PBS with 0.01% Tween 20, and gently shaken under 37°C. At different time points, the microspheres were imaged using an inverted research microscope and a laser confocal microscope to track their degradation.

9.8 | Cellular Viability of pMS

The 3-(4,5-dimethylthiazol-2-yl)-2,5-diphenyl tetrazolium bromide (MTT) assay was used to evaluate the cellular viability of pMS. Briefly, DC 2.4 and MLE 12 cells were seeded in 96-well plates at the density of 10^4 cells per well. 12 h later, different concentrations of pMS were added to the plates and cultured for another 24 h. Then, the cellular viability was evaluated using a standard MTT assay.

9.9 | Biosafety Evaluation of pMS In Vivo

To evaluate the potential impact of pMS on respiratory function, the breath rate and arterial O_2 saturation were monitored by a small animal pulse oximeter (MouseOx, STARR Life Sciences) at 1-, 7-, 14-, and 30-days post-administration of pMS. Besides, lung tissues were collected from vaccinated mice 28 days after administration, fixed in 4% paraformaldehyde, and subjected to H&E staining to assess the tissue for any signs of damage.

9.10 | In Vitro Immunostimulation

To assess the in vitro immunostimulatory of microspheres, bone marrow-derived dendritic cells (BMDCs) isolated from C57BL/6 mice were cultured in 24-well non-treated plate and cultured with pMS containing OVA, pMS containing MPLA, free OVA with MPLA, pMS containing OVA and MPLA, or lipopolysaccharide (LPS). 24 h later, BMDCs were harvested and stained with FITC-anti-CD11c (BioLegend, 117306), PE-anti-CD80 (BioLegend, 104708), APC-anti-H^2K^b bound to SIINFEKL (BioLegend, 141606) and PE-CY7-anti-CD86 (BioLegend, 105014). for BMDCs maturation and cross-presentation using flow cytometry (Fongcytes, Challenbio). Meanwhile, the supernatant was collected to analyze the levels of IL-6 (Dakewe Biotech, 1210603), IL-12p70 (ThermoFisher, 88-7121-88), and TNF-α (ThermoFisher, 88-7324-88) using ELISA kits.

For in vitro T-cell proliferation analysis, CD 8^+ T cells were isolated from the spleen of OT-1 mice, and stained with the CellTrace CFSE cell proliferation kit (Invitrogen) according to standard protocol. Then, the treated BMDCs (10^4) were co-cultured with CSFE-labeled T cells (10^5) in the round-bottom 96-well plate (Beyotime) for 72 h, and cell proliferation was analyzed using flow cytometry (Fongcytes, Chellenbio).

9.11 | In Vivo Immune Responses

At predetermined days post-vaccination, vaccinated mice were sacrificed, and the lung and mediastinal lymph nodes were collected and processed into single-cell suspensions. These suspensions were all stained with anti-CD16/32 (BioLegend, 101302) to block Fc receptors. The lung and colon-derived single cells were stained with APC-anti-CD103 (BioLegend, 110906), FITC-anti-CD3 (BioLegend, 100204), BV605-anti-CD69 (BioLegend, 104530), PE-anti-CD44 (BioLegend, 163610), APC-CY7-anti-CD8 (BioLegend, 100714), and PE-CY7-anti-CD4 (BioLegend, 100422) according to the manufacturer's instructions. The lymph nodes-derived single cells were stained with Apc-anti-GL7 (BioLegend, 144617), PE-anti-B220 (BioLegend, 103207), PE-CY7-anti-CD95 (BioLegend, 152617), FITC-anti-CD38 (BioLegend, 102705), FITC-anti-CD3 (BioLegend, 100204), PE-CY7-anti-CD4 (BioLegend, 100422), APC-anti-PD1 (BioLegend, 143710), PE-anti-CXCR5 (BioLegend, 145503), APC-CY7-anti-ICOS (BioLegend, 313529) according to manufacturee's instructions.

The spleen was also collected and homogenized to form a single-cell suspension. The red blood cells were lysed with red blood cell lysis buffer. Splenocytes were cultured with OVA257-254 peptide (10 μg /mL, GenScript) in the presence of brefeldin A (BioLegend, 420601), for 8 h, then stained with APC-CY7-anti-CD8 (BioLegend, 100714), PE-CY7-anti-CD4 (BioLegend, 100714), PE-anti-IFNγ (BioLegend, 505808), APC-anti-IL2 (BioLegend, 503809), FITC-anti-CD3 (BioLegend, 100204), and Percp-anti-CD45 (BioLegend, 103130) according to manufacturer's instructions. Finally, the cells were measured by flow cytometry (Fongcytes, Chellenbio, and BD FACSAria III, BD Biosciences)

9.12 | Antibody Titer Measurement

Serum from immunized mice was collected at predetermined time points and stored at −80°C for further analysis. OVA was coated onto ELISA plates overnight at 4°C. The plate was washed with PBST (1 × PBS with 0.01% Tween 20) to remove unbound OVA and blocked with ELISA diluent (Thermo Fisher Scientific) for 2 h. After washing, serial dilutions of serum were added and incubated for 2 h. Plates were then washed again and incubated with horseradish peroxidase (HRP)-conjugated anti-mouse immunoglobulin (HRP-IgG at 1: 10 000, Abcam; HRP-IgA at 1: 8000, SouthernBiotech) for 1 h. Finally, the wells were washed with PBST for five times and incubated with TMB substrate (APExBIO, K1131, USA), and colorimetric detection was

performed using a multimode microplate reader (Synergy H1, Bio Tek). The antibody titer was determined as the highest dilution factor at which the absorbance value exceeded twofold that of the blank control at equivalent dilution.

9.13 | In Vivo Antitumor Assay

In B16-OVA prevention models, female C57BL/6 mice were inhaled with pMS vaccine (10 mg/kg antigen and 50 μg/kg MPLA) and Free vaccine (10 mg/kg antigen and 50 μg/kg MPLA). 28 days post-immunization, the mice were intravenously injected with 5×10^5 B16-OVA cells. 18 days post cancer cell injection, the mice were sacrificed, and their lungs were weighed, and the metastatic foci were counted. In the long-term anti-metastasis experiment, female C57BL/6 mice were immunized with pMS vaccine (10 mg/kg antigen and 50 μg/kg MPLA) and Free vaccine (10 mg/kg antigen and 50 μg/kg MPLA). 361 days post-immunization, the mice were intravenously injected with 3×10^5 B16-OVA cells. 40 days after injection, the mice were sacrificed, and the lungs were weighed, and the metastatic foci were counted.

In the LLC-Luc local model, local tumors were established by intravenous injection of 8×10^5 LLC-Luc tumor cells. The tumor antigen was extracted from LLC-Luc cells by Nonidet P-40 and purified before loading into liposomes and pMS to construct the vaccine. 5-day post-injection, mice were inhaled with Free vaccine, liposome vaccine, and pMS vaccine (10 mg/kg antigen and 50 μg/kg MPLA). Besides, the intradermal injection of the liposome vaccine was also performed as a standard vaccine formulation. The bioluminescence was continuously monitored to indicate tumor growth. 23 days post-vaccination, mice were sacrificed. The lungs and mediastinal lymph nodes were collected and processed as described above to further evaluate the therapeutic ability.

In the postoperative metastasis model, the 2×10^6 4T1-Luc tumor cells were injected into the breast pad of the mice. 15-day post-injection, surgical resection was performed to remove the tumor. The tumor antigen was extracted from the resected tumor by Nonidet P-40 and purified before loading into liposomes and pMS to construct the vaccine. The mice were randomly allocated into different treatment groups, including inhalation with the liposome vaccine and pMS vaccine (10 mg/kg antigen and 50 μg/kg MPLA). The bioluminescence was continuously monitored to indicate tumor growth. 22 days post-vaccination, mice were sacrificed. The lungs and mediastinal lymph nodes were collected and processed as described above to further evaluate the therapeutic ability.

In the patient-derived xenograft (PDX) tumor model, the humanized mice were established by intravenous injection of human peripheral blood mononuclear cells (hPBMC) into NOD-Prkdc^{scid} Il2rg^{tm1}/Cavens mice two weeks before use. Patient's pulmonary tumor tissue was acquired from patients in Shanghai Pulmonary Hospital after obtaining informed consent, and was used under good clinical practice approved by the China Food and Drug Administration (CFDA). Fresh tumor tissue (after surgical resection) was kept in growth medium and cut into pieces (~2–4 mm) in a sterile dish. The tumor pieces were then implanted onto the chest of each humanized mouse under general anaesthesia using forceps. The skin incision was closed using an absorbable suture. The tumor antigen was extracted from the tumor by Nonidet P-40 and purified before loading into liposomes and pMS to construct the vaccine. One day post-implantation, humanized mice were inhalated with liposome vaccine and pMS vaccine. The tumor was continuously monitored with a vernier caliper. 11 weeks post-inhalation, mice were sacrificed and tumors were collected to evaluate the infiltration of immune cells.

9.14 | Histological Analysis and Immunofluorescence Staining

Following different treatments, the lung tissues of mice were collected and fixed in 4% paraformaldehyde for Hematoxylin and Eosin (H&E) staining and immunostaining. For H&E staining, organ sections were stained with Mayer's hematoxylin solution and eosin Y solution. Images were captured using an inverted research microscope (Ts2R, Nikon). For immunostaining, organs were embedded with optimal cutting temperature (OCT) compound and sectioned into frozen slices using the freezing microtome (CM1860, Leica). Immunofluorescence staining was performed using anti-CD8 (Proteintech, 29896-1-AP) for lung tissue staining, or AF647-anti-GL7 (BioLegend, 144605) and AF488-anti-B220 (BioLegend, 103228) for lymph node staining. The stained sections were then imaged using laser confocal imaging (LSM 800, Zeiss).

9.15 | Immunological Memory Responses

At predetermined days post-vaccination, peripheral blood cells were collected from vaccinated mice. Red blood cells were lysed using red blood cell lysis buffer (Solarbio, R1010). The remaining peripheral blood cells were then stained with the following antibodies according to the manufacturer's instructions: APC-CY7-anti-CD8 (BioLegend, 100714), PE-CY7-anti-CD4 (BioLegend, 100422), PE-anti-CD44 (BioLegend, 163610), APC-anti-CD62L (BioLegend, 161217), and FITC-anti-CD3 (BioLegend, 100204). Subsequently, the stained peripheral blood cells were analyzed by flow cytometry (Fongcyte, Chellenbio).

9.16 | Statistical Analysis

Data are presented as the mean ± standard deviation (SD). Tukey post hoc tests and one-way ANOVA were used for multiple comparisons (when more than two groups were compared), and Student's t-test was used for two-group comparisons. All statistical analyses were performed with the Prism software package (PRISM 10.0.0; GraphPad Software). All schemes were drawn by Biorender. Experimental groups show significant differences when $*p < 0.05$, $**p < 0.01$, $***p < 0.001$, and $****p < 0.0001$.

Acknowledgements

This article was partially supported by the National Research Programs of China (No. 2022YFA1206500), the National Natural Science Foundation of China (Nos. 52450010, 52325106 and 52271248), the Collaborative Innovation Center of Suzhou Nano Science and Technology, the Suzhou Key

Laboratory of Nanotechnology and Biomedicine, and the 111 Program from the Ministry of Education of China.

Conflicts of Interest

The authors declare no conflicts of interest.

Data Availability Statement

The data that support the findings of this study are available from the corresponding author upon reasonable request.

References

1. S. Cobey, "Vaccination Against Rapidly Evolving Pathogens and the Entanglements of Memory," *Nature Immunology* 25 (2024): 2015–2023, https://doi.org/10.1038/s41590-024-01970-2.

2. D. Gouglas, T. Thanh Le, K. Henderson, et al., "Estimating the Cost of Vaccine Development Against Epidemic Infectious Diseases: A Cost Minimisation Study," *The Lancet Global Health* 6 (2018): e1386–e1396.

3. E. C. Lavelle and R. W. Ward, "Mucosal Vaccines — Fortifying the Frontiers," *Nature Reviews Immunology* 22 (2022): 236–250.

4. J. Holmgren and C. Czerkinsky, "Mucosal Immunity and Vaccines," *Nature Medicine* 11 (2005): S45–S53.

5. O. Kocabiyik, P. Amlashi, A. L. Vo, et al., "Vaccine Targeting to Mucosal Lymphoid Tissues Promotes Humoral Immunity in the Gastrointestinal Tract," *Science Advances* 10 (2024): adn7786.

6. A. Iwasaki, "Exploiting Mucosal Immunity for Antiviral Vaccines," *Annual Review of Immunology* 34 (2016): 575–608.

7. S. W. Zhang, D. A. Edwards, R. Langer, and K. Cheng, "Inhalable Materials and Biologics for Lung Defence and Drug Delivery," *Nature Reviews Materials* 11 (2026): 90–116.

8. Z. Wang, K. D. Popowski, D. Zhu, et al., "Exosomes Decorated With a Recombinant SARS-CoV-2 Receptor-Binding Domain as an Inhalable COVID-19 Vaccine," *Nature Biomedical Engineering* 6 (2022): 791–805.

9. T. Ye, Z. Jiao, X. Li, et al., "Inhaled SARS-CoV-2 Vaccine for Single-Dose Dry Powder Aerosol Immunization," *Nature* 624 (2023): 630–638.

10. J. Wang, P. Li, Y. Yu, et al., "Pulmonary Surfactant–Biomimetic Nanoparticles Potentiate Heterosubtypic Influenza Immunity," *Science* 367 (2020): aau0810.

11. B. L. Hartwell, M. B. Melo, P. Xiao, et al., "Intranasal Vaccination With Lipid-Conjugated Immunogens Promotes Antigen Transmucosal Uptake to Drive Mucosal and Systemic Immunity," *Science Translational Medicine* 14 (2022): abn1413.

12. G. Stary, A. Olive, A. F. Radovic-Moreno, et al., "A Mucosal Vaccine Against Chlamydia Trachomatis Generates Two Waves of Protective Memory T Cells," *Science* 348 (2015): aaa8205.

13. L. Yao, G. Zhang, Y. Wang, et al., "Development of an Inhalable DNA Tetrahedron MicroRNA Sponge," *Advanced Materials* 37 (2025): 2414336.

14. F. Wegmann, K. H. Gartlan, A. M. Harandi, et al., "Polyethyleneimine is a Potent Mucosal Adjuvant for Viral Glycoprotein Antigens," *Nature Biotechnology* 30 (2012): 883–888.

15. X. Li, M. Xu, J. Yang, et al., "Multifunctional Nanoparticle-Mediated Combining Therapy for Human Diseases," *Signal Transduction and Targeted Therapy* 9 (2024): 1.

16. J. Yang, M.-Q. Liu, L. Liu, et al., "A Triple-RBD-Based Mucosal Vaccine Provides Broad Protection Against SARS-CoV-2 Variants of Concern," *Cellular & Molecular Immunology* 19 (2022): 1279–1289.

17. H. Lei, W. Hong, J. Yang, et al., "Multifunctional Nanoparticle-Mediated Combining Therapy for Human Diseases," *Signal Transduction and Targeted Therapy* 9 (2024): 1.

18. E. K. Wasan, J. Syeda, S. Strom, et al., "A Lipidic Delivery System of a Triple Vaccine Adjuvant Enhances Mucosal Immunity Following Nasal Administration in Mice," *Vaccine* 37 (2019): 1503–1515.

19. Q. Jin, W. Zhu, J. Zhu, et al., "Nanoparticle-Mediated Delivery of Inhaled Immunotherapeutics for Treating Lung Metastasis," *Advanced Materials* 33 (2021): 2007557.

20. D. Horonushi, A. Yoshida, Y. Nakata, et al., "Membrane Backtracking at the Maximum Capacity of Nondigestible Antigen Phagocytosis in Macrophages," *Biophysical Journal* 122 (2023): 2707–2726.

21. D. A. Edwards, J. Hanes, G. Caponetti, et al., "Large Porous Particles for Pulmonary Drug Delivery," *Science* 276 (1997): 1868–1872.

22. A. Brandwood, K. R. Noble, and K. Schindhelm, "Phagocytosis of Carbon Particles by Macrophages In Vitro," *Biomaterials* 13 (1992): 646–648.

23. J. Löndahl, W. Möller, J. H. Pagels, W. G. Kreyling, E. Swietlicki, and O. Schmid, "Measurement Techniques for Respiratory Tract Deposition of Airborne Nanoparticles: A Critical Review," *Journal of Aerosol Medicine and Pulmonary Drug Delivery* 27 (2014): 229–254.

24. C. C. Wang, K. A. Prather, J. Sznitman, et al., "Airborne Transmission of Respiratory Viruses," *Science* 373 (2021): abd9149.

25. K. Rakhra, W. Abraham, C. Wang, et al., "Exploiting Albumin as a Mucosal Vaccine Chaperone for Robust Generation of Lung-Resident Memory T Cells," *Science Immunology* 6 (2021): abd8003.

26. B. J. Baaten, C.-R. Li, and L. M. Bradley, "Multifaceted Regulation of T Cells by CD44," *Communicative & Integrative Biology* 3 (2010): 508–512.

27. S. H. Bhagchandani, L. Yang, J. H. Lam, et al., "Two-Dose Priming Immunization Amplifies Humoral Immunity by Synchronizing Vaccine Delivery With the Germinal Center Response," *Science Immunology* 9 (2024): adl3755.

28. M. Z. Syeda, T. Hong, C. Huang, W. Huang, and Q. Mu, "B Cell Memory: From Generation to Reactivation: A Multipronged Defense Wall Against Pathogens," *Cell Death Discovery* 10 (2024): 117.

29. D. Tarlinton, "B-Cell Lymphomas: Getting in the Zone!," *Blood* 120 (2012): 2158–2159.

30. Z. Shulman, A. D. Gitlin, S. Targ, et al., "T Follicular Helper Cell Dynamics in Germinal Centers," *Science* 341 (2013): 673–677.

31. B. Grimbacher, A. Hutloff, M. Schlesier, et al., "Homozygous Loss of ICOS is Associated With Adult-Onset Common Variable Immunodeficiency," *Nature Immunology* 4 (2003): 261–268.

32. P. T. Sage, L. M. Francisco, C. V. Carman, and A. H. Sharpe, "The Receptor PD-1 Controls Follicular Regulatory T Cells in the Lymph Nodes and Blood," *Nature Immunology* 14 (2013): 152–161.

33. J. S. Weinstein, E. I. Herman, B. Lainez, et al., "TFH Cells Progressively Differentiate to Regulate the Germinal Center Response," *Nature Immunology* 17 (2016): 1197–1205.

34. J. Merkenschlager, R.-M. Berz, V. Ramos, et al., "Continually Recruited Naïve T Cells Contribute to the Follicular Helper and Regulatory T Cell Pools in Germinal Centers," *Nature Communications* 14 (2023): 6944.

35. H. Aegerter, B. N. Lambrecht, and C. V. Jakubzick, "Biology of Lung Macrophages in Health and Disease," *Immunity* 55 (2022): 1564–1580.

36. B. Button, L.-H. Cai, C. Ehre, et al., "A Periciliary Brush Promotes the Lung Health by Separating the Mucus Layer from Airway Epithelia," *Science* 337 (2012): 937–941.

37. B. Eshaghi, A. Schudel, I. Sadeghi, et al., "The Role of Engineered Materials in Mucosal Vaccination Strategies," *Nature Reviews Materials* 9 (2024): 29–45.

38. D. J. Mooney, J. Kim, W. A. Li, et al., "Injectable, Spontaneously Assembling, Inorganic Scaffolds Modulate Immune Cells In Vivo and Increase Vaccine Efficacy," *Nature Biotechnology* 33 (2015): 64–72.

39. H. Hao, S. Wu, J. Lin, et al., "Immunization Against Zika by Entrapping Live Virus in a Subcutaneous Self-Adjuvanting Hydrogel," *Nature Biomedical Engineering* 7 (2023): 928–942, https://doi.org/10.1038/s41551-023-01014-4.

40. G. Ma, X. Xi, T. Ye, et al., "Self-Healing Microcapsules Synergetically Modulate Immunization Microenvironments for Potent Cancer Vaccination," *Science Advances* 6 (2020): aay7735.

Supporting Information

Additional supporting information can be found online in the Supporting Information section.

Supporting File: adma72696-sup-0001-SuppMat.docx.